Dedicated to Academician Aureliu Sandulescu's 80^{th} Anniversary

REFRACTIVE VERSUS RESONANT DIFFRACTION SCATTERING OF LOOSELY BOUND NUCLEI

FLORIN CARSTOIU[1], ŞERBAN MIŞICU[1], LIVIUS TRACHE[1,2]

[1]"Horia Hulubei" National Institute for Physics and Nuclear Engineering,
POB-MG6, Bucharest-Măgurele, RO-077125, Romania, EU
Email: carstoiu@theory.nipne.ro
[2]Cyclotron Institute, Texas A& M University, College Station, TX 77843-3366, USA
Email: l-trache@tamu.edu

Received October 27, 2011

We present a complete analysis of elastic scattering ^{6}Li+^{16}O at 4 MeV/nucleon. Using either traditional Woods-Saxon or a range of semi microscopic folding form factors we find that the data require deep, highly transparent potentials. The intermediate angle structures and the oscillatory increase of the cross section at large angles is interpreted either as a pre-rainbow oscillation resulting from the interference of the barrier and internal barrier far-side scattering subamplitudes, or, equally well, as a resonant diffraction arising from two Regge poles located in peripheral waves. Both semiclassical and Regge pole approaches allow a dynamical separation of the resonant component of the S-matrix.

PACS: 25.70.Bc, 24.10.Ht, 25.70.Hi, 27.20.+n.

1. INTRODUCTION

The study of nucleus-nucleus elastic scattering has a long history but remains of interest due to both successes and failures that mark it (see for example, Refs. [1, 2] and references therein). We are searching here for reliable ways to predict optical model potentials for reactions with radioactive nuclear beams (RNB). In particular our interest focuses on finding reliable descriptions for transfer and breakup reactions involving relatively light, loosely bound nuclei, which are used in indirect methods in nuclear astrophysics. A range of RNB studies were made at energies around 10 MeV/nucleon, where the reactions are peripheral, with the intent to obtain information about stellar reaction rates. These reactions use DWBA techniques to extract nuclear structure information. However, the well known existence of many ambiguities in the optical potential model (OMP) extracted from elastic scattering can raise questions about the accuracy of these determinations. Experimental studies using RNBs have, heretofore, not been suitable for detailed elastic scattering analyses. The best information comes from studying the elastic scattering of stable loosely bound nuclei with similar mass. We chose here to study the elastic scattering of ^{6}Li at low energy, a fragile projectile (loosely bound), with a pronounced cluster structure and

with low Z. At this energy a range of phenomena, involving absorption, resonant diffraction and refraction, mostly of nuclear nature, can be exhibited.

Previously we have carried out a study of elastic scattering around 10 MeV/nucleon for a range of projectile-target combinations involving p-shell nuclei [3,4]. We found a relatively simple method to predict OMP for loosely bound nuclei, based on the renormalization of the independent real and imaginary terms obtained from a double folding procedure using the JLM nucleon-nucleon (NN) effective interaction. The procedure successfully described the data for all projectile-target combinations and energies in the study for most of the angular ranges measured.

Recent work [5,6] has established that elastic scattering of light, tightly-bound heavy ion systems such as ^{16}O+^{12}C and ^{16}O+^{16}O show sufficient transparency for the cross section to be dominated by the far-side scattering. Intermediate angle structures appearing in the elastic scattering distributions at angles beyond the Fraunhofer diffractive region have been identified as Airy minima of a nuclear rainbow, *i.e.* a destructive interference between two far-side trajectories which samples the interior of the potential. A number of high order Airy minima have been identified by observing that such structures are largely insensitive to an artificial reduction of the absorption in the optical potential, and therefore they appear as a manifestation of the refractive power of the nuclear potential. While at high energy [7] this picture was well substantiated by a semiclassical nonuniform decomposition of the scattering function [8], at lower energies the situation is more difficult to understand. It has been shown by Anni [9], that such structures could be explained by the interference of two amplitudes appearing in different terms of a multireflection uniform series expansion of the scattering amplitude and therefore the interpretation using rainbow terminology is not appropriate.

For loosely bound nuclei at low energy the situation is even more intricate. The corresponding components in the optical potential are expected to be more diffuse as compared to normal nuclei, leading to a competition between the increased refractive power of the real potential and the increased absorption at the nuclear surface. The small separation energy implies also that the dynamic polarization potential (DPP) [10] arising from the coupling to breakup states may be strong and have a complicated energy and radial dependence. Thus the DPP cannot be treated as a small perturbation for loosely bound nuclei and the usual phenomenological procedure in renormalizing the folding potential form factor may be questioned. It has been estimated that the DPP is strongly repulsive at the nuclear surface in the case of ^{6}Li [11]. This prompted Mahaux, Ngo and Satchler [12] to conjecture that for loosely bound nuclei the barrier anomaly may be absent due to the cancellation between the repulsive (DPP) and attractive (dispersive) components of the optical potential.

In the specific case of ^{6,7}Li scattering on light targets, a large body of data has been accumulated in the range 4-50 MeV/nucleon. At high energy, Nadasen and his

group [13,14] have been able to derive a unique optical potential which was essential to assess the quality of the folding model. At lower energies, ambiguities found in the analysis of data prevented any definite conclusion about the strength and energy dependence of the optical potential. A study by Trcka *et al.* [15] on ^{6}Li+^{12}C elastic scattering at 50 MeV, found an exotic feature ("plateau") in the angular distribution of the elastic scattering at intermediate angles which resembles similar structures found in more bound systems. They interpreted the structure as a diffractive effect arising from an angular momentum dependent absorption. There are experimental hints that such structures also appear in neighboring systems, ^{6}Li+^{16}O and ^{6}Li+^{9}Be, as a possible manifestation of the average properties of the interaction potential.

In this paper we present an analysis of elastic scattering of ^{6}Li on ^{16}O at 4 MeV/nucleon. Accurate angular distribution has been measured over an almost complete angular range [16]. This angular distribution displays a complex structure at intermediate and large angles pointing to strong refractive effects.

Folding model analysis using the complex, density and energy dependent NN interaction of Jeukenne, Lejeune and Mahaux (JLM) [17], as well as other G-matrix effective interactions, where corrections due to the strong DPP have been included, confirmed that the elastic distribution could be described using deep and extremely transparent potentials. The intermediate angle structures have been discussed using the semiclassical uniform approximation for the scattering function of Brink and Takigawa [18]. We explain the intermediate angle structure as a coherent interference effect of two subamplitudes corresponding to trajectories reflected at the barrier and interfering with trajectories which sample the nuclear interior. Thus, this refractive effect appears as a signature of a highly transparent interaction potential. A completely different picture emerges using a phenomenological Regge pole analysis [19], pointing to a resonant effect present in surface waves.

The paper is structured in the following way: after this introduction, the analysis of the elastic scattering data using phenomenological and microscopic optical model potentials is presented in Sect. 2. In Sect. 3 we present a discussion of the decomposition of the far-side scattering amplitude into barrier and internal barrier components responsible for the exotic structure at intermediate angles. Finally we perform a Regge pole analysis in Sect. 4), and conclude our work in Sect. 5).

2. OPTICAL-MODEL ANALYSIS

The ratio of the measured elastic scattering data to the Rutherford cross section at E_{lab}=25.7 MeV [16], covers a large angular range, see Fig.2. These data show complex forms with characteristic rapid oscillations at small angles followed by a marked change in shape at intermediate angles: a plateau develops at $\theta = 75^{\circ} - 135^{\circ}$ which is followed by a significant increase of the cross section at larger angles, re-

membering the well known ALAS. Assuming pure Fraunhofer scattering at forward angles, we extract a grazing angular momentum, $l_g \approx 12$, from the angular spacing $\Delta\theta = \pi/(l_g + 1/2)$.

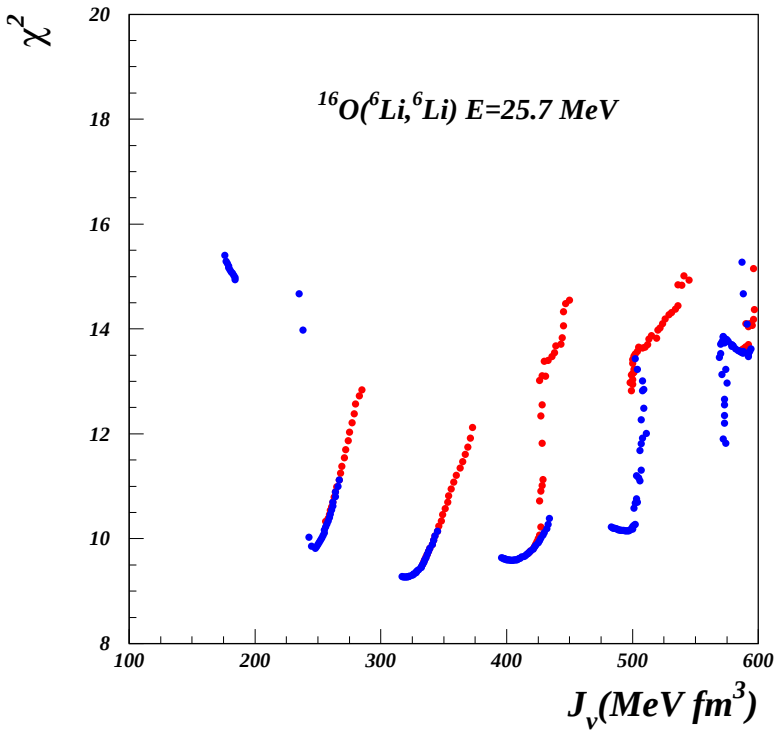

Fig. 1 – (Color online) Discrete ambiguities in the WS optical potential obtained from a grid search on the real volume integral. There are no acceptable solutions with $J_V < 200$ MeV fm^3. Best solutions are tabulated in Table 1.

The data are analyzed using optical potentials with conventional Woods-Saxon (WS) form factors for the nuclear term, supplemented with a Coulomb potential generated by a uniform charge distribution with a reduced radius fixed to r_c=1 fm. No preference has been found for volume or surface localized absorption and throughout the paper only volume absorption is considered. In the absence of any spin dependent observables, spin-orbit or tensor interactions have been ignored. Ground state reorientation couplings also have been neglected. The potential is defined by six parameters specifying the depth and geometry of the real and imaginary terms, with the standard notations, the same as used in Ref. [3]. The number of data points is N=99 and therefore the usual goodness of fit criteria (χ^2) normalized to N has been used. The averaging associated with the finite angular resolution has mostly an effect

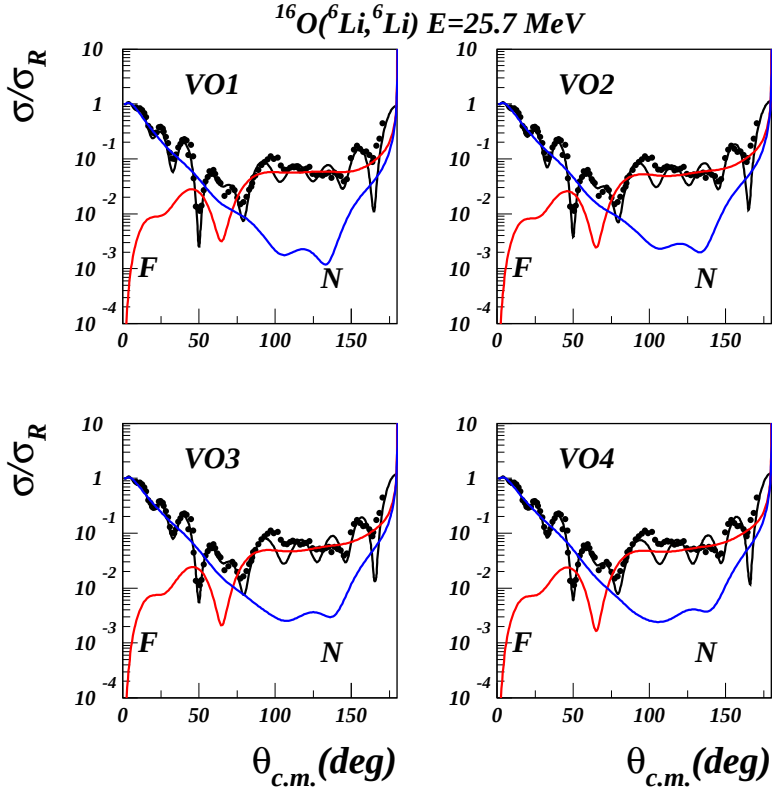

Fig. 2 – (Color online) Woods-Saxon optical model analysis (full lines) of elastic scattering data (open points) at 4 MeV/nucleon (Table 1). Far-side (red line)and near-side(blue line) cross sections are also shown.

on the depth of sharp minima. A few exploratory calculations showed that allowing the normalization to vary did not result in any qualitative changes and did not indicate that any renormalization of the data by more than a few percent would be preferred. Optical parameter sets obtained in our previous paper [4] were used as starting values for the search procedure. Guided by these potentials and by our earlier analysis [3] a number of some 10^4 potentials with real volume integrals in the range $J_V = 200 - 600$ MeV fm^3 have been generated, thus exploring the functional Woods-Saxon space in full detail. Local minima were identified and a complete search on all six parameters determined the best fit potentials. The complex structure at intermediate angles and the increase of the cross section at large angles could be described only with deep potentials with real volume integrals (per pairs of interacting nucleons) exceeding a critical value $J_{V\,\mathrm{crit}} \approx 240$ MeV fm^3. We did not find any acceptable solution with $J_V < 200$ MeV fm^3 (see Fig. 1). There is a consistent pref-

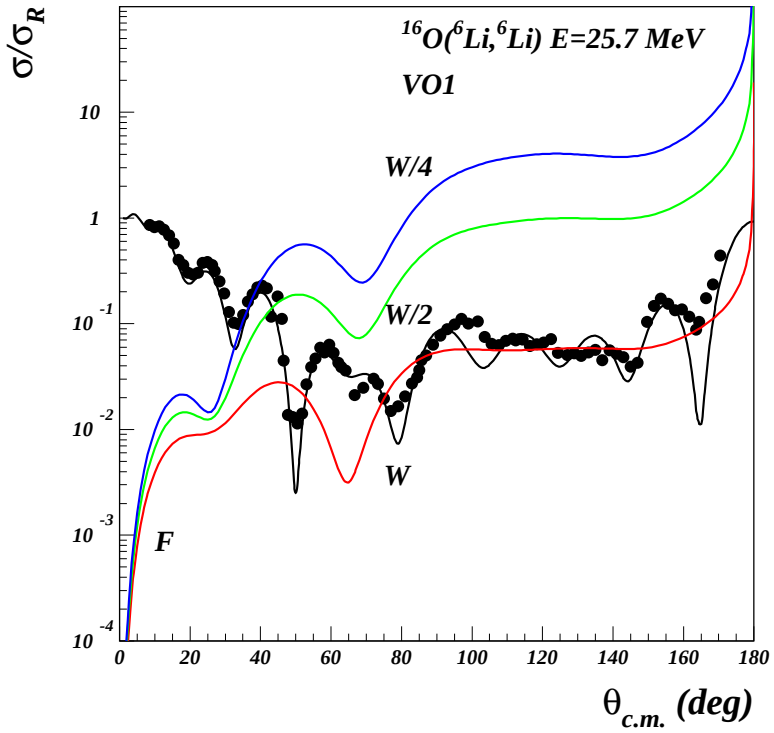

Fig. 3 – (Color online) Evolution of the far side component with the nominal absorption in the VO1 parametrization of the WS potential The stable minimum at $\theta \approx 65^{\circ}$ may be interpreted as a primary Airy minimum of a nuclear rainbow.

erence for potentials with very weak imaginary parts, with values of W around 5-7 MeV. We systematically find $r_V < r_W$ and large diffuseness parameters $a_V \simeq a_w \simeq 0.8$ fm in agreement with theoretical expectations for loosely bound nuclei [20, 21]. A grid search procedure on the real depth of the potential allowed us to identify discrete ambiguities. Parameters for the first four discrete families are given in Table 1. These are identified by a jump of $\Delta J_V \approx 100$ MeV fm^3 from one family to the next and an almost constant imaginary volume integral. As a consequence, the total reaction cross section seems to be a well determined observable. Grinding on other WS parameters revealed a continuous ambiguity of the form $J_V R_V \approx$ const, where R_V is the rms radius of the potential. The larger the volume integral, the smaller the radius that is required to fit the data. This is a clear manifestation of a complicated radial dependence of the dynamic polarization potential (DPP) which may lead to radii much smaller than the minimal value implied by the folding model (e.g., $R_F^2 = R_1^2 + R_2^2$, for a zero range NN effective interaction). However, for each discrete family rather precise values of the rms radii were required to fit both forward and intermediate

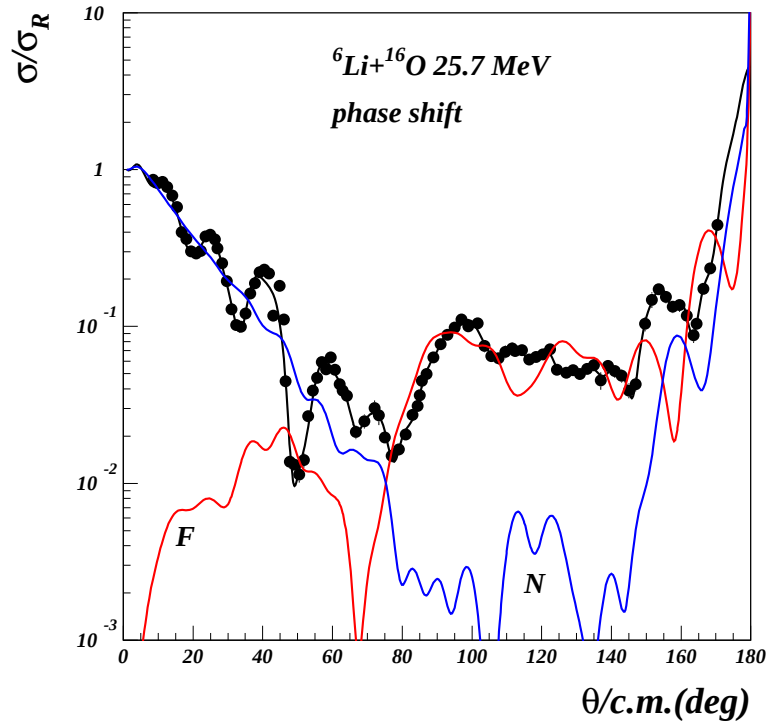

Fig. 4 – (Color online) Phase shift analysis. The fluctuations in the near side cross section arise from the noise present in the data.

angle cross sections.

As mentioned already, it was shown in Refs. [5–7] that the elastic scattering of light heavy ion systems such as ^{16}O+^{12}C and ^{16}O+ ^{16}O shows sufficient transparency for the cross section to be dominated by far-side scattering. Structures appearing in the elastic scattering angular distributions at intermediate angles have been identified as Airy minima of a nuclear rainbow, due to a destructive interference between two far-side trajectories which sample the interior of the potential. At 4 MeV/nucleon the ^{6}Li scattering data show rapid, diffractive Fraunhofer oscillations at forward angles due to the strong near-far amplitude interference (Fig. 2). At $\theta \approx 48^\circ$ the far side and near side components of the scattering amplitude are almost equal, producing the first Fraunhoffer deep minimum. Beyond this "crossover" the near-side amplitude makes a negligible contribution and the cross section is dominated by the far side component. There is no dark side exponential decay of the far side component. The deep minimum seen at $\theta \approx 65^\circ$ in the far side component is stable against the strength of the absorption (Fig. 3) and may be interpreted as a primary Airy minimum of a nuclear rainbow. It is followed by a broad Airy maximum and a structureless increase of

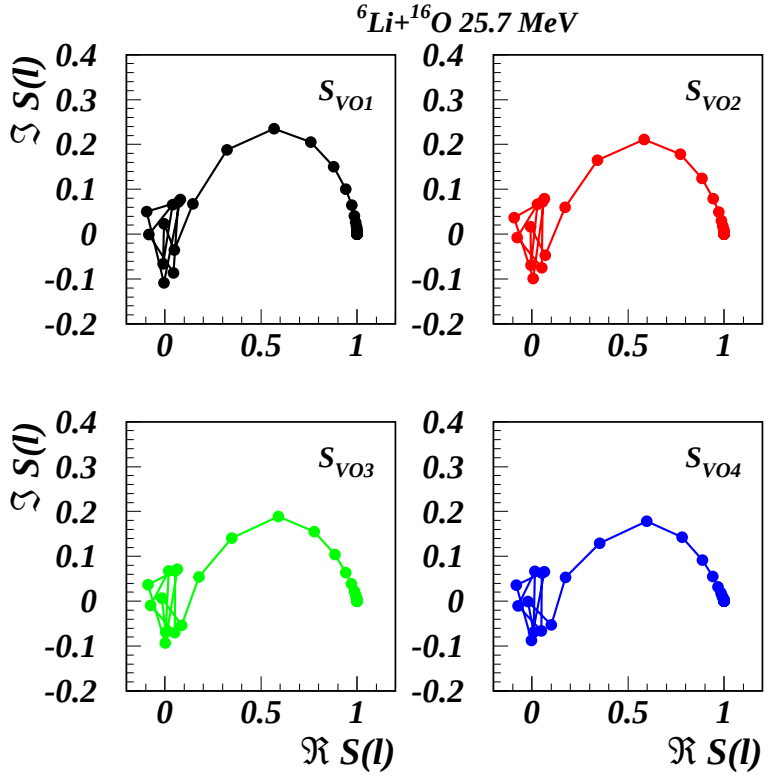

Fig. 5 – (Color online) Argand diagrams for the WS S-matrix. Optical potentials are from Table 1. For low angular momentum $l < 10$, the trajectory for S-matrix rotates clockwise several times around the origin, suggesting the presence of several Regge poles.

the far side cross section at large angles. Low amplitude oscillation of the total cross section at intermediate and large angles are due to far side /near side interference. The total cross section reaches a maximum near $\theta = 180^\circ$ where both components became again equal. Clearly, far-side dominance may be interpreted as a possible manifestation of refractive effects. However, this simple dominance does not explain, by itself the structure of the far side component. In fact the above picture has already been challenged by Anni [9] and by Michel *et al.* [22] for the simple reason that the far-side amplitude has never been decomposed in subamplitudes which would explain the interference. We come back to this topic in Section 3. For the moment we adopt the interpretation of Michel *et al.* [22] and denote the complex structure at intermediate angles in the data as pre-rainbow oscillations. A model independent analysis in which the diagonal S-matrix elements are extracted directly from the data through a complex phase shift analysis confirm that the Airy oscillation at $\theta \approx 65^\circ$ is a real effect (see Fig. 4). Further information can be obtained by looking at the

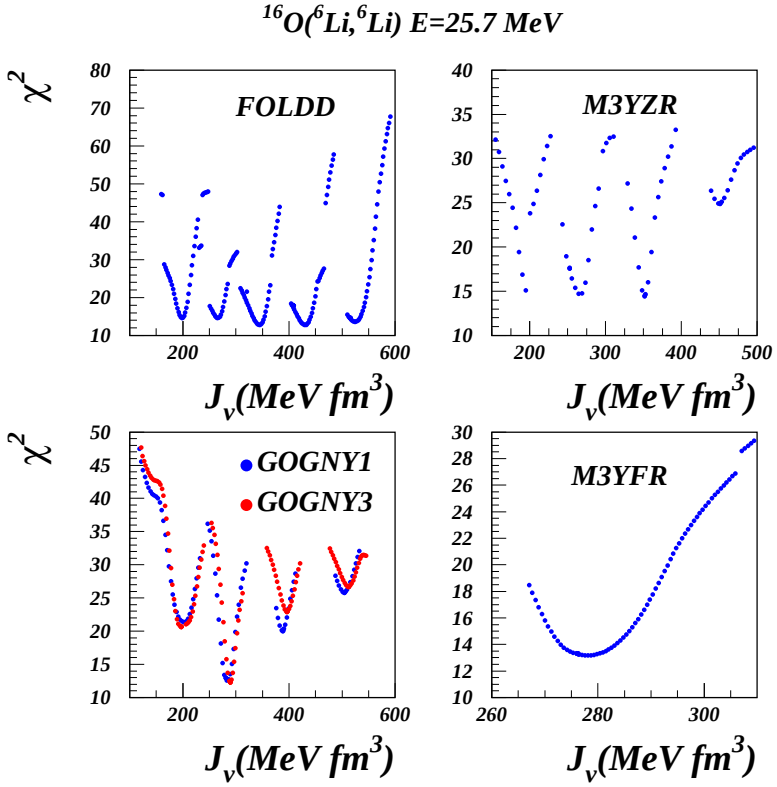

Fig. 6 – (Color online) Discrete ambiguities for folding potentials. The FOLDD and M3YZR models predict several solutions which describe equally well the data, while GOGNY and M3YFR predict a unique solution with $J_V \sim 280$ MeV fm^3.

Argand diagrams displayed in Fig. 5. It demonstrates that the discrete potentials VOi (i=1-4) Table 1 are fully equivalent since the Argand patterns are almost identically for all potentials. It means that the Drisko ambiguity [23], $\delta_l \rightarrow \delta_l + n\pi$ holds not only for low angular momenta but for all momenta when going from one potential to another. Furthermore, for low angular momentum $l < 10$, the trajectory for S-matrix rotates clockwise several times around the origin, suggesting the presence of several Regge poles. We will come back to this effect in the following sections.

2.1. FOLDING MODEL ANALYSIS

In the this section we discuss the ability of the folding model to describe the pre-rainbow oscillation seen in our data.

We start by a quite simple model, dubbed here FOLDD in which the form

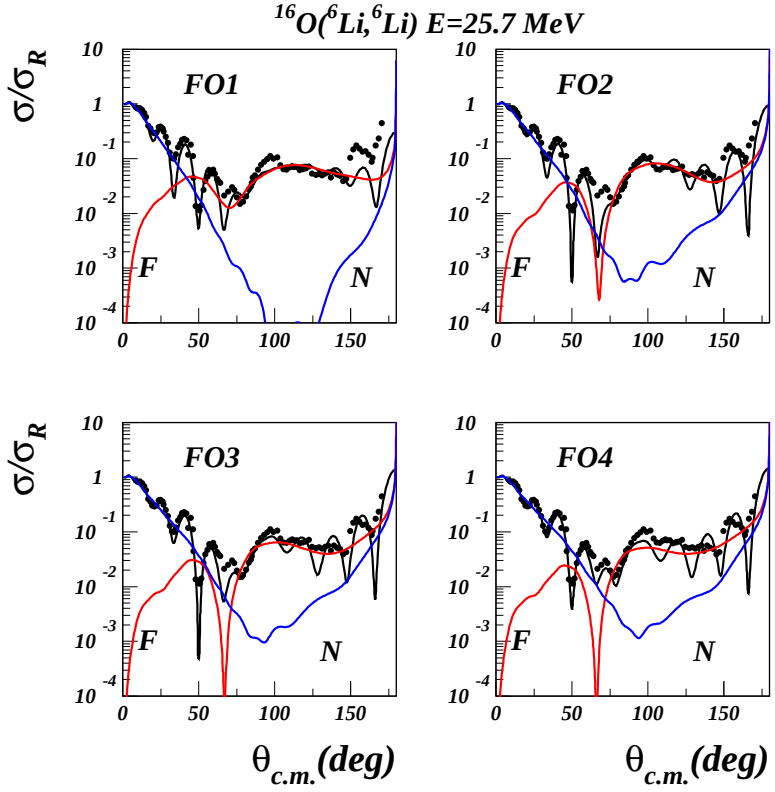

Fig. 7 – (Color online) Cross sections calculated with a simple zero range double folding potential Strengths and ranges are tabulated in Table 3

factors of the OMP are given by a simple δ-folding potential,

$$V_{fold}(R) = \int d\vec{r}_1 d\vec{r}_2 \rho_1(r_1)\rho_2(r_2)\delta(\vec{s}) \tag{1}$$

where $\vec{s} = \vec{r}_1 + \vec{R} - \vec{r}_2$. No exchange terms are included in this model which is intended mainly to check the single particle densities and the mechanism behind the discrete ambiguities found with the WS model. Then the OMP is given by,

$$U(R) = N_V V(R, t_V) + N_W W(R, t_W) \tag{2}$$

where $N_{V,W}$ are normalization constants and $t_{V,W}$ are range parameters of a smearing function g,

$$g(\vec{s}) = \frac{1}{t^3 \pi^{3/2}} \exp(-s^2/t^2) \tag{3}$$

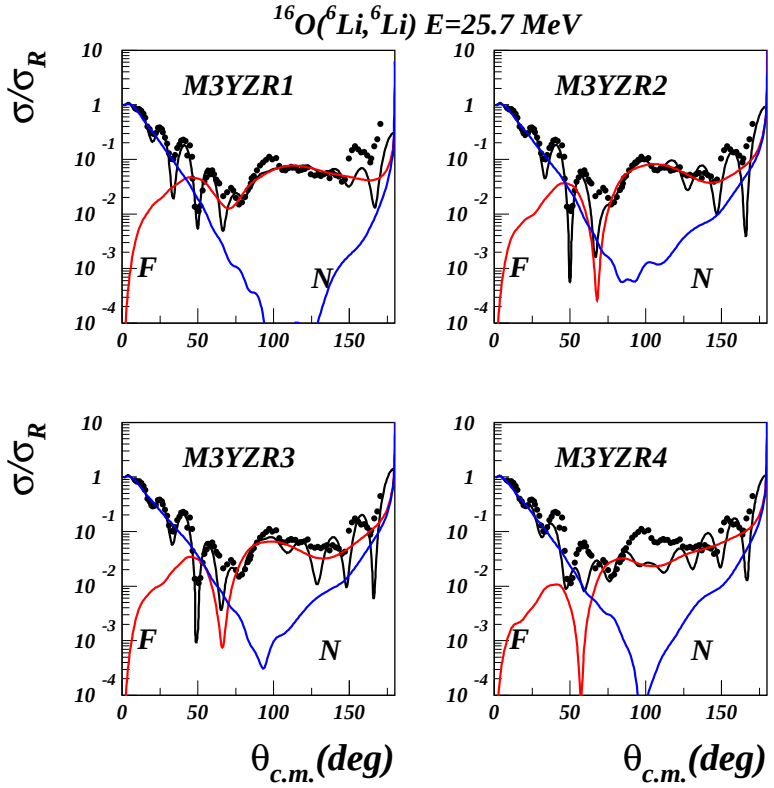

Fig. 8 – (Color online) Cross sections calculated with the zero range version of the M3Y effective interaction. . Renormalization parameters and rages are given in Table 3.

With this function, the form factors of the OMP are given by,

$$V(R,t_V) = \int d\vec{R}' V_{fold}(R') g(\vec{R} - \vec{R}') \tag{4}$$

and similarly for $W(R,t_W)$. Note that the normalized function g goes to a δ function in the limit $t \to 0$. The rms radius of the OMP form factor is given by,

$$< r^2 >_V = < r^2 >_{\rho_1} + < r^2 >_{\rho_2} + \frac{3}{2} t^2 \tag{5}$$

Thus the volume integral of the form factor is controlled by the parameters $N_{V,W}$. Based on Eq.(5) one may estimate in an average way the importance of the dynamic polarization potential and finite range effects. Throughout this paper we use single particle densities obtained from a spherical Hartree-Fock calculation based on the density functional of Beiner and Lombard [24]. The obtained rms charge radii are $< r^2 >^{1/2}_{^6\mathrm{Li}} = 2.33$ fm and $< r^2 >^{1/2}_{^{16}\mathrm{O}} = 2.71$, which should be compared with the

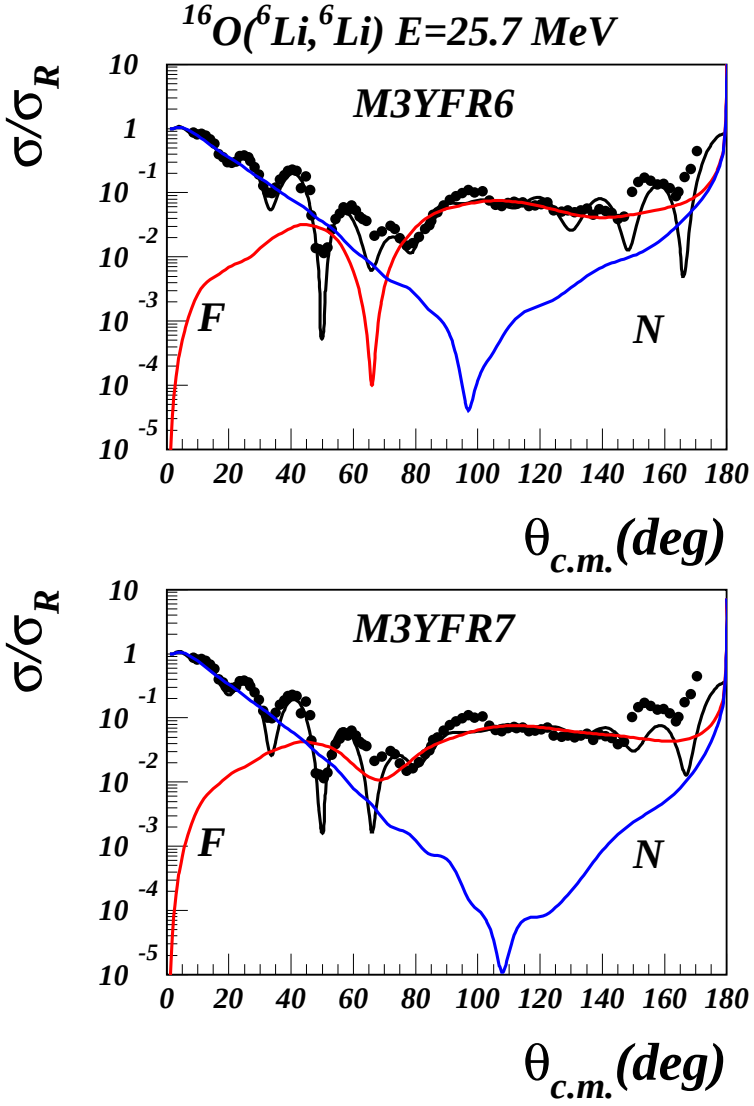

Fig. 9 – (Color online) Cross sections calculated with the finite range version of the M3Y effective interaction. Renormalization parameters and rages are given in Table 3.

experimental values of 2.53 fm and 2.70 fm, respectively [25]. A grid search on the real volume integral reveals the same ambiguity obtained with the WS form factors, see Fig.6. The real volume integrals match quite well solutions found with the WS parametrization. Again imaginary volume integrals are quite small pointing to a large transparency of the potential. Correction due to the finite range effects are quite large,

of the order of $\Delta r \approx 0.4$ fm for the real potential and even larger for the imaginary potential. Far side / near side decomposition of the scattering amplitude reveals the same features: a minimum in the far side component develops at $\theta = 65^\circ$ which becomes deeper with the increased real volume integral of the interaction.

Finite range effects can be conveniently taken into account by using the M3Y parametrization of the G-matrix obtained from the Paris NN interaction [26]. In this case the direct term reads

$$V_{fold}(R) = \int d\vec{r}_1 d\vec{r}_2 \rho_1(r_1)\rho_2(r_2) v_{M3Y}(s) \tag{6}$$

In the zero range approximation, the exchange term is simulated by a zero-range pseudo-potential in the form of Eq. (1) with a strength slightly energy dependent,

$$J_{00}(E) = -276(1 - 0.005E/A) \tag{7}$$

Results of these calculations are dubbed M3YZR and displayed in Table 3 and Fig. 8. The same pattern emerges as in the case of the FOLDD model except that we did not found acceptable solutions with $J_V > 400$ MeV fm^3.

A more elaborate calculation lead to a nonlocal knock-on exchange kernel,

$$U_{ex}(\vec{R}^+, \vec{R}^-) = \mu^3 v_{ex}(\mu R^-) \int d\vec{X}_1 \rho_1(X_1) \hat{j}_1(k_{f1}(X_1) \frac{(A_1-1)A_2}{A_1+A_2} R^-) \\ \times \rho_2(|\vec{R}^+ - \vec{X}_1|) \hat{j}_1(k_{f2}(|\vec{R}^+ - \vec{X}_1|) \frac{(A_2-1)A_1}{A_1+A_2} R^-) \tag{8}$$

where $A_{1,2}$ are mass numbers, μ is the reduced mass of the system, $k_{f1,2}$ are Fermi momenta, $R^{+,-}$ are the usual nonlocal coordinates and v_{ex} is the exchange component of the interaction including the long range OPEP tail. In the lowest order of the Perey-Saxon approximation, the local equivalent of the nonlocal kernel is obtained by solving the nonlinear equation,

$$U_L(R) = 4\pi \int d\vec{r}_1 d\vec{r}_2 \rho_1(r_1)\rho_2(r_2) \\ \times \int s^2 ds v_{ex}(s) \hat{j}_1(k_{f1}(r_1)\beta_1 s) \hat{j}_1(k_{f2}(r_1)\beta_2 s) j_0(\frac{1}{\mu} K(R) s) \delta(\vec{r}_2 - \vec{r}_1 + \vec{R}) \tag{9}$$

Above $\beta_i = (A_i - 1)/A_i$ are recoil corrections and the local momentum for the relative motion is given by,

$$K^2(R) = \frac{2\mu}{\hbar^2}(E_{c.m.} - U_D(R) - U_L(R)) \tag{10}$$

where U_D is the total direct component of the potential including the Coulomb term. In Eq. (10) we assumed a purely real local momentum of the relative motion since the absorptive component of the OMP is small compared with the real part. The effective mass correction [27], $\frac{\mu^\star}{\mu} = 1 - \frac{\partial U}{\partial E}$ is of the order of a few percent for this system

and is absorbed in the renormalization parameter N_W. Some tens of iterations are needed to solve eq.(9) in order to obtain a precision of 10^{-7} in the entire radial range. Calculations with this model are dubbed M3YFR. As in the case of other interactions it is possible to find several solution. Two of them are displayed in Fig. 9. However, a careful calculation reveals that in fact there is an *unique* solution with $J_V = 280$ MeV fm^3 (Fig. 6). Thus the approximate calculation of the knock-on exchange component changes completely the volume integral and the rms radius of the real component such that a unique solution survives in the range $J_V = 250 - 300$ MeV fm^3.

At this point we want to make a comment on the effect of coupling with the breakup states. Sakuragi [11] performed a CCDC calculation of ^{6}Li scattering in a large range of incident energies and target mass. He found that coupling with $\alpha - d$ breakup states brings a repulsive DPP potential in the nuclear surface in such a way that reasonable fits can be obtained by fixing the normalization constant $N_V = 1$ and $N_W = 0.4 - 0.7$ when using the M3Y effective interaction supplemented by a pseudo zero range knock-on potential as we did in our model M3YZR. First of all he assumes implicitly that M3Y is a perfect interaction and the renormalization N_V should be exactly one. This is not the case for several reasons. Absence of any explicit density dependence and of three body effects leads to a collapse of nuclear matter equation of state at least at the HF level. The pseudo potential used for the knock-on exchange is a poor approximation. The odd components (SO and TO) of the interaction are largely ambiguous. We have seen that in a single channel calculation there are discrete ambiguities with real volume integrals $J_V = 200 - 350$ MeV fm^3. The bare (unnormalized) potential has a volume integral of 425 MeV fm^3 and a rms radius of 3.86 fm. It means that the DPP potential coming from coupling to breakup should correct simultaneously the volume integral by $\Delta J_V = 225, 165, 80$ MeV fm^3 and for $\Delta R_V = 0.1 - 0.2$ fm which is evidently impossible. Furthermore, in line with our previous analyses [3, 4] we found systematically $\Delta R = R_W - R_V \approx 1.4$ fm and therefore it is a bad approximation to use the same geometry for real and absorptive components of the OMP.

Is this unique solution an accidental feature of the M3YFR model? In a recent paper [28] we successfully described the hindrance in the sub-barrier fusion of ^{48}Ca with several targets using optical potentials generated with two parametrization of the Gogny effective interaction. Neglecting the spin-orbit component, the Gogny NN interaction can be expressed as a sum of central, finite range term and a zero range density dependent term,

$$v(\vec{r}_{12}) = \sum_{i=1}^{2}(W_i + B_i P_\sigma - H_i P_\tau - M_i P_\sigma P_\tau) e^{(-r_{12}^2/\mu_i^2)} + t_3(1 + P_\sigma)\rho^\alpha(\vec{R}_{12})\delta(\vec{r}_{12}) \quad (11)$$

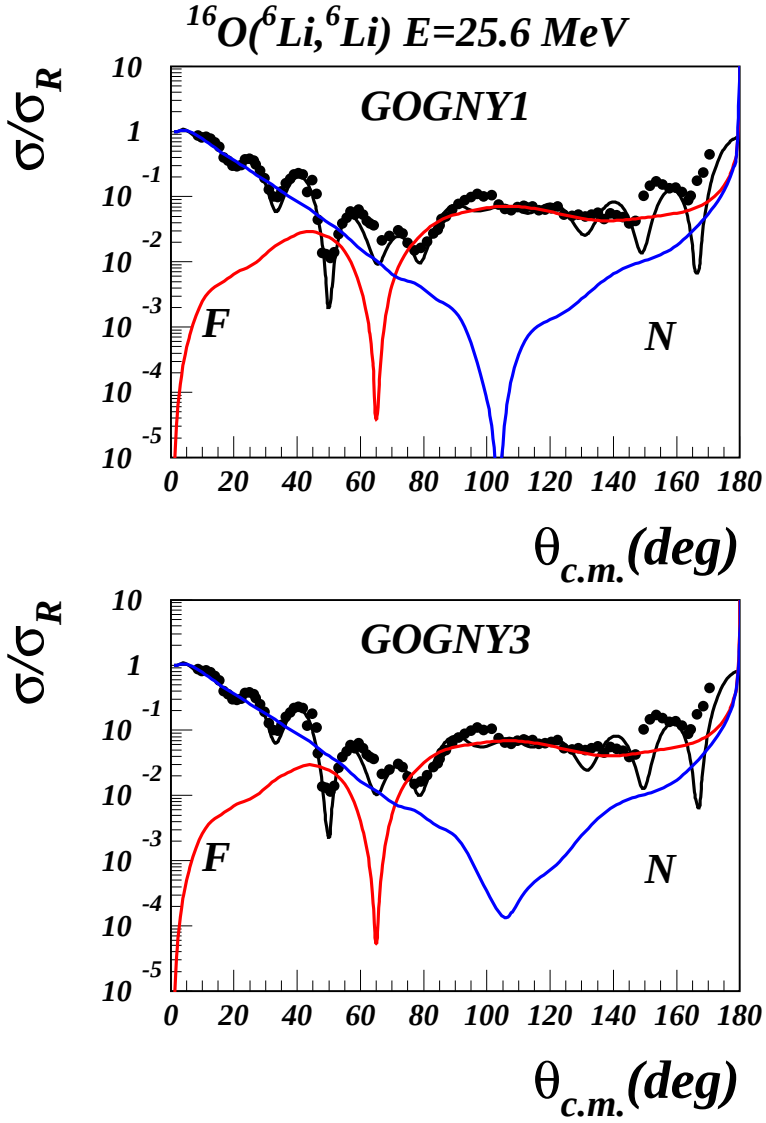

Fig. 10 – (Color online) Cross sections calculated with D1 parametrization of the Gogny effective interaction. Renormalization parameters and rages are given in Table 2.

where $\vec{r}_{12} = \vec{r}_1 - \vec{r}_2$, $\vec{R}_{12} = (\vec{r}_1 + \vec{r}_2)/2$ and standard notations have been used for strengths parameters and spin-isospin exchange operators. The strengths and the ranges are taken from [29]. Antisymmetrization of the density dependent term is

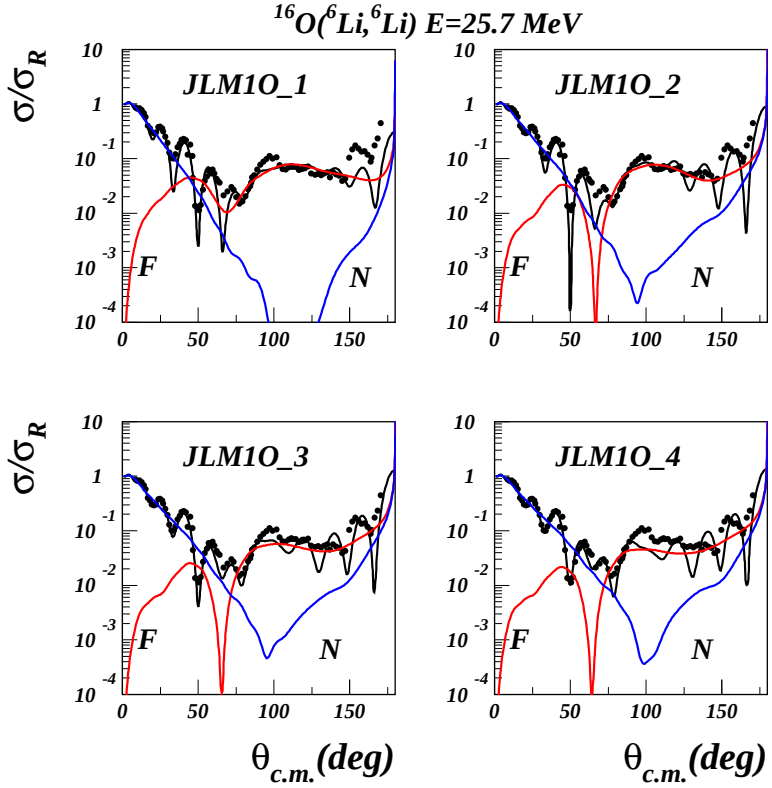

Fig. 11 – (Color online) Cross sections calculated with JLM1O effective interaction. Renormalization parameters and rages are given in Table 2.

trivial, so that the sum of direct and exchange term reads,

$$v_D^\rho(r_{12}) + v_{ex}^\rho(r_{12}) = \frac{3t_3}{4}\rho^\alpha\delta(\vec{r}_{12}) \tag{12}$$

The local equivalent of the finite range knock-on exchange is calculated with eq. (9). Two approximations were used for the overlap density,

$$\rho = (\rho_1(r_1)\rho_2(r_2))^{1/2} \tag{13}$$

and

$$\rho = \frac{1}{2}(\rho_1(r_1) + \rho_2(r_2)) \tag{14}$$

The first approximation eq.(13) has the merit that the overlap density goes to zero when one of the interacting nucleons ar far from the bulk. The calculated OMP potentials are dubbed GOGNY1 and GOGNY3 respectively. Both definitions represent crude approximations of the overlap density but are widely used in the estimation of the density effects in the folding model. Several solutions have been found with this

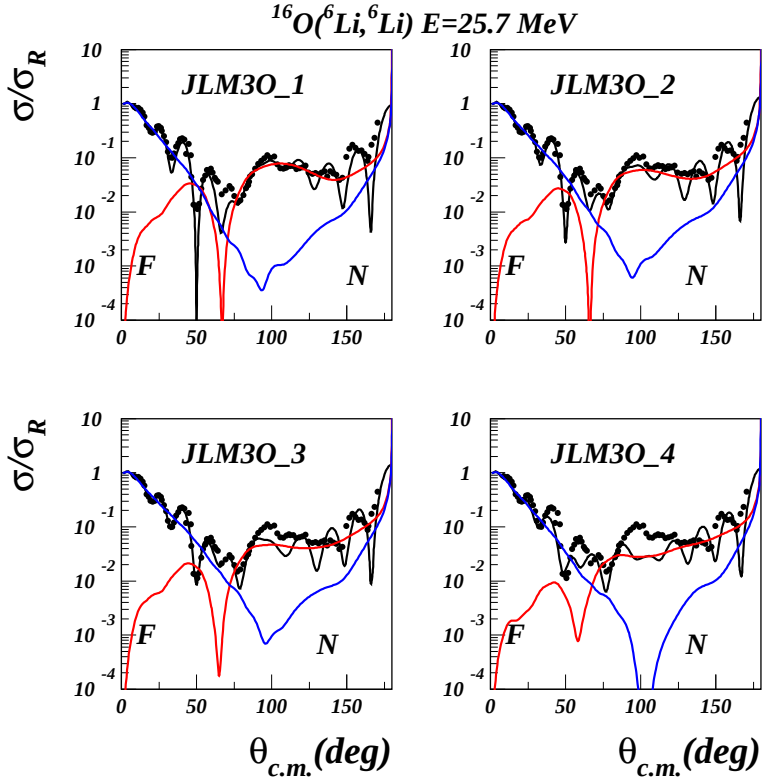

Fig. 12 – (Color online) Cross sections calculated with JLM3O effective interaction. Renormalization parameters and rages are given in Table 2.

model, but in fact only one give a fit comparable with best solutions found with other form factors (Fig. 6 and Fig.10). Estimation with the overlap density defined in eqs. (13) or (14) do not make too much difference (table 2). Both approximations lead to the same volume integrals and rms radii.

We further examine the density dependence effects by using the nuclear matter approach of Jeukenne, Lejeune and Mahaux (JLM) [17] which incorporates a complex, energy and density dependent parametrization of the NN effective interaction obtained in a Brueckner Hartree-Fock approximation from the Reid soft core nucleon-nucleon potential. The systematic study [3] of the elastic scattering between p-shell nuclei at energies around 10 MeV/nucleon led to the surprising result that on average, the imaginary part of the folded JLM potential was perfectly adequate to describe such reactions and did not need any renormalization ($N_W = 1.00 \pm 0.09$), while the real component needed a strong renormalization, in line with other effective interactions used in folding models. We do not expect this property to be conserved

at much lower energy (4 MeV/A in this case). Calculations with this model are dubbed JLM1O and JLM3O, depending on which definition we use for the overlap density(eqs.(9) and (10) respectively) and the results are tabulated in Table 2 and displayed in Figs. 11 and 12. There are no exchange components included in this model and as a consequence several discrete solutions are found. Renormalization parameter N_V lies in the range 0.4-0.7 in line with all other calculations. Values close to N_V=0.9 tend to underestimate the shoulder at $\theta \approx 100^\circ$ since the near side component of the amplitude has a deep minimum in this region.

To conclude this section, we find that folding potentials describe well the cross section in the entire angular range, comparable with the more flexible WS form factors. Inclusion of the more elaborated knock-on exchange potential reduces the number of discrete ambiguities, while the dynamical content of the S-matrix remains the same, with strong resonant effect in the low partial waves (see Fig. 13).

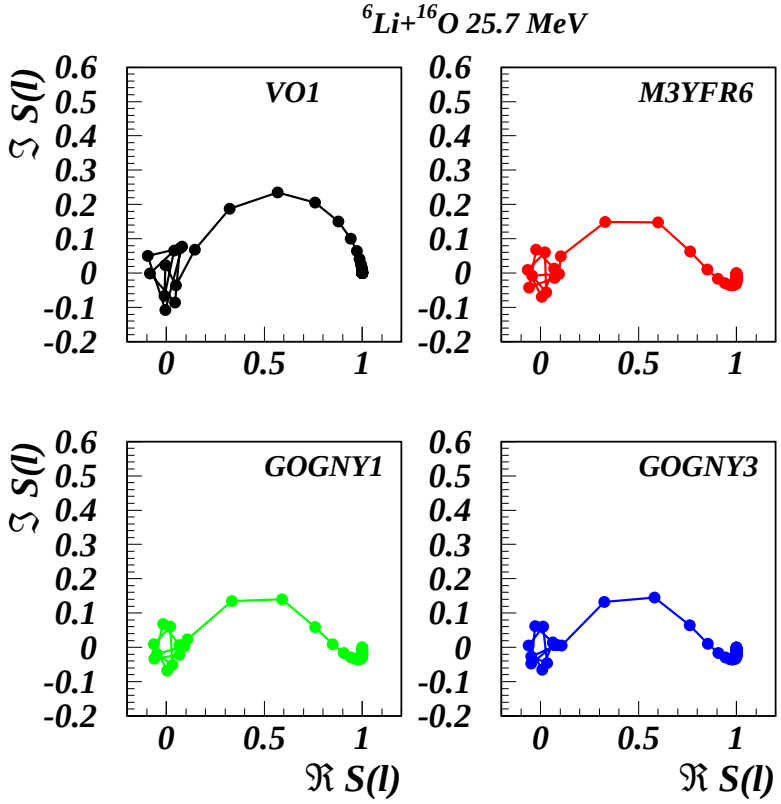

Fig. 13 – (Color online) Argand diagrams for VO1, M3YFR6, GOGNY1 and GOGNY3 parametrizations of the optical potential.

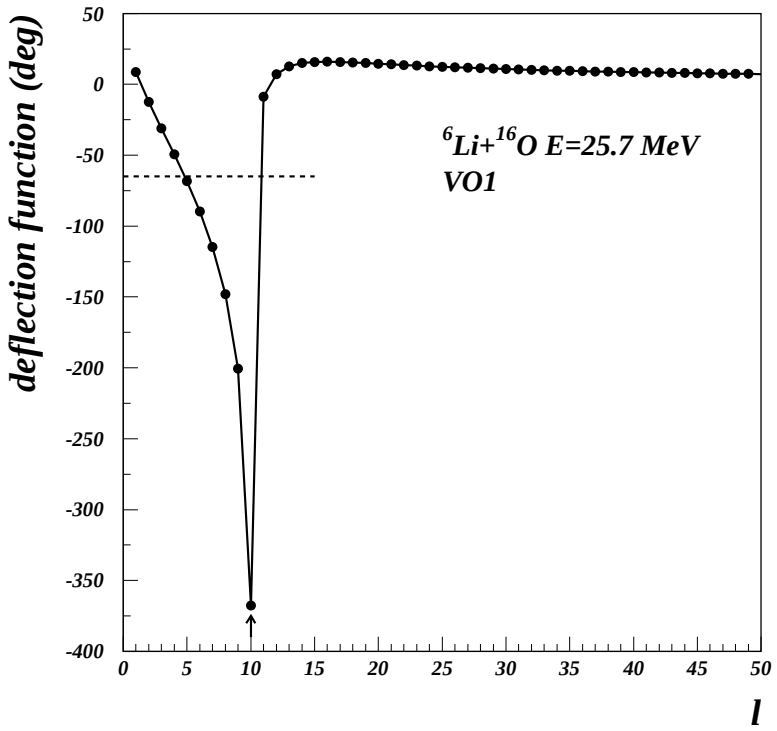

Fig. 14 – Semiclassical deflection function using the VO1 parametrization of the bare WS potential. The shape is asymmetric and has a logarithmic singularity at the orbiting momentum $l \approx 10$. The dashed line at $\theta = -65^\circ$ marks the position of the Airy minimum. The arrow marks the orbiting angular momentum.

3. SEMICLASSICAL BARRIER AND INTERNAL BARRIER AMPLITUDES

Once we have established the main features of the average OM potential, we turn now to study the reaction mechanism using semiclassical methods. The far-side dominance observed in the angular distributions is not able to explain the behaviour of the S-matrix elements at low angular momentum. The reason is of course that the far/near (F/N) decomposition method does not perform a dynamic decomposition of the scattering function, but merely decomposes the scattering amplitude into traveling waves. The intermediate angle structures, such as those observed in our angular distribution, have been repeatedly interpreted as arising from the interference of two ranges in angular momenta, $\ell_<$ and $\ell_>$, contributing to the same negative deflection angle. However, the corresponding cross sections, $\sigma_{F<}$ and $\sigma_{F>}$, cannot be isolated because their dynamic content (S-matrix) is not accessible.

The semiclassical uniform approximation for the scattering amplitude of Brink and Takigawa [18] is well adapted to describe situations in which the scattering is

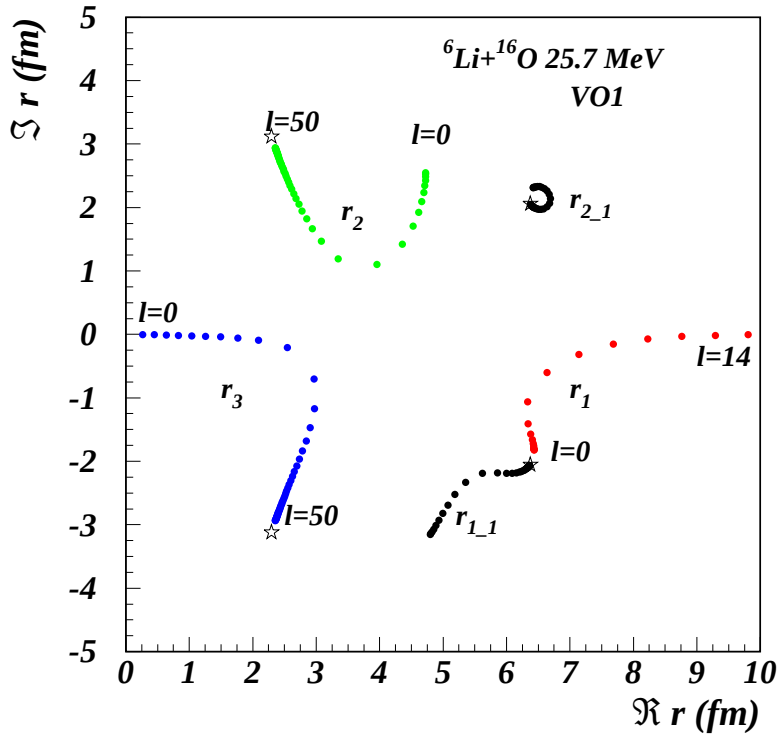

Fig. 15 – (Color online) Trajectories of complex turning points for the potential VO1,Table 1. Inactive turning points r_{1-1} and r_{2-1} are plotted with black points. The complex poles of the potential are plotted with stars.

controlled by at most three active, isolated, complex turning points. An approximate multireflection series expansion of the scattering function can be obtained, the terms of which have the same simple physical meaning as in the exact Debye expansion for the scattering of light on a spherical well. The major interest in this theory comes from the fact that it can give precious information on the response of a nuclear system to the nuclear interior. Recent application [9] of this technique helped to clarify the controversial problem of the "Airy oscillation" seen in low energy ^{16}O+^{12}C scattering [5].

We take as an example the potential VO1 in Table 1. We discard the absorptive term and define the effective potential as,

$$V_{eff}(r) = V(r) + \frac{\hbar^2}{2\mu}\frac{\lambda^2}{r^2}, \quad \lambda = \ell + \frac{1}{2} \tag{15}$$

where the Langer prescription has been used for the centrifugal term. This guarantees the correct behavior of the semiclassical wave function at the origin [30]. Then we

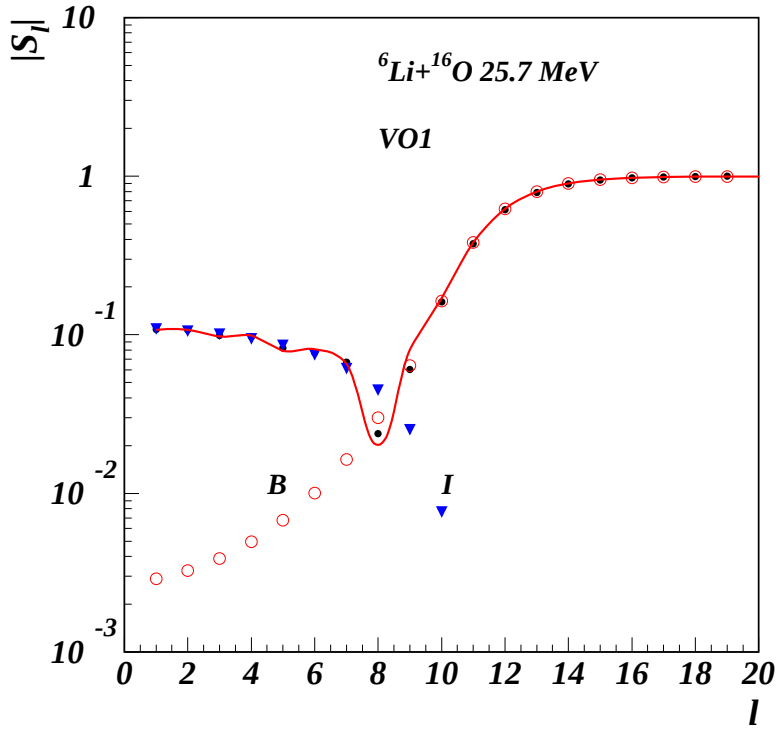

Fig. 16 – (Color online) Semiclassical absorption profile for the WS potential VO1. Barrier (open circles) and internal barrier components (triangles) are indicated. The exact total quantum S-matrix is indicated by small dots. The line is a cubic spline interpolation of the total semiclassical scattering function for the same potential. The Grühn-Wall deep at $l \sim 8$ appears as an interference between barrier and internal barrier amplitudes

calculate the deflection function,

$$\Theta(\lambda) = \pi - 2\int_{r_1}^{\infty} \frac{\sqrt{\frac{\hbar^2}{2\mu}}\lambda dr}{r^2\sqrt{E_{c.m.} - V_{eff}}} \tag{16}$$

where r_1 is the outer zero of the square root, *i.e.* the radius of closest approach to the scatterer and μ is the reduced mass. Note that with the replacement $\hbar\lambda = b\sqrt{2\mu E}$, Eq. 16 becomes identical with the classical deflection function $\Theta(b)$, where b is the impact parameter. The result is shown in Fig. 14. The behavior of $\Theta(\lambda)$ is the one expected for a strong nuclear potential in a *near orbiting* kinematical situation in which the c.m. energy approximately equals that of the top of the barrier for some specific angular momentum. All the measured angular range is classically illuminated. The deflection function exhibit no genuine minima, but rather a pronounced cusp close to an orbiting logarithmic singularity. Therefore any interpretation of

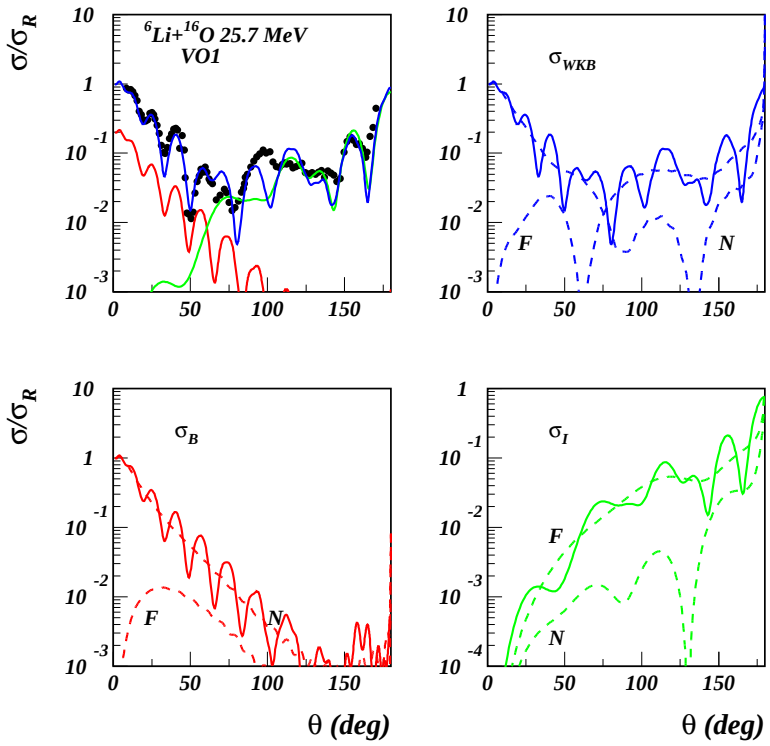

Fig. 17 – (Color online) Semiclassical calculation for the potential VO1, Table 1. The total cross section (blue line) is decomposed into barrier (σ_B, red line) and internal barrier (σ_I, green line). Each cross section is also decomposed into far side (F) and near side (N) component.

structures in angular distributions in terms of Airy oscillations can be discarded. Rather we need an interpretation appropriate for orbiting, a well documented situation in classical physics [31]. We identify the cusp angular momentum as orbiting momentum (λ_o) since this is related to the coalescence of two (barrier) turning points and the innermost turning point given by the centrifugal barrier becomes classically accessible. There are two branches that can be distinguished, an internal branch for low active momenta $\lambda < \lambda_o$ related to semiclassical trajectories which penetrate into the nuclear pocket and a less developed external (barrier) branch ($\lambda > \lambda_o$) related to trajectories deflected at the diffuse edge of the potential.

However this simple calculation cannot determine the relative importance of these branches and provides no information about the interference effects of the corresponding semiclassical trajectories. To clarify these points it is best to go into the complex r-plane and look for complex turning points, *i.e.* the complex roots of the quantity $E_{c.m.} - V_{eff} - iW$. This is an intricate numerical problem, because, for a

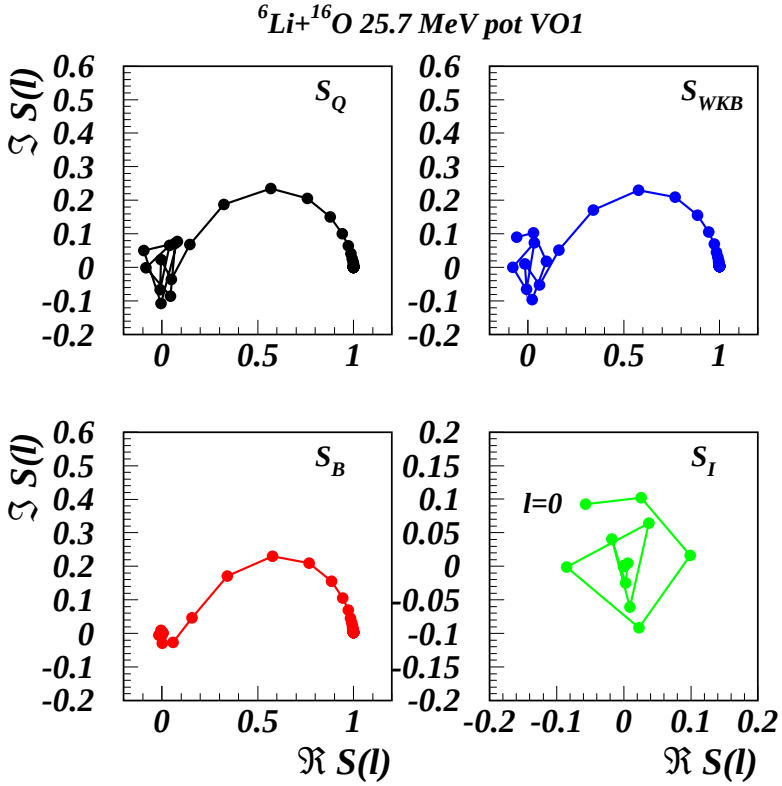

Fig. 18 – (Color online) Argand diagrams for the exact S-matrix (S_Q) calculated with WS potential VO1 compared with WKB approximations for the same potential. Barrier S_B and internal-barrier S_I components are shown separately.

WS optical potential, the turning points are located near the potential singularities and there are an infinite number of such poles. The situation for integer angular momenta is depicted in Fig. 15. Active turning points nearest the real axis are plotted with color symbols. We observe an ideal situation with three, well isolated, turning points for each partial wave.

The multireflection expansion of the scattering function in the Brink-Takigawa approach reads,

$$S_{WKB}(\ell) = \sum_{q=0}^{\infty} S_q(\ell) \tag{17}$$

where,

$$S_0(\ell) = \frac{\exp(2i\delta_1^{\ell})}{N(S_{21}/\pi)} \tag{18}$$

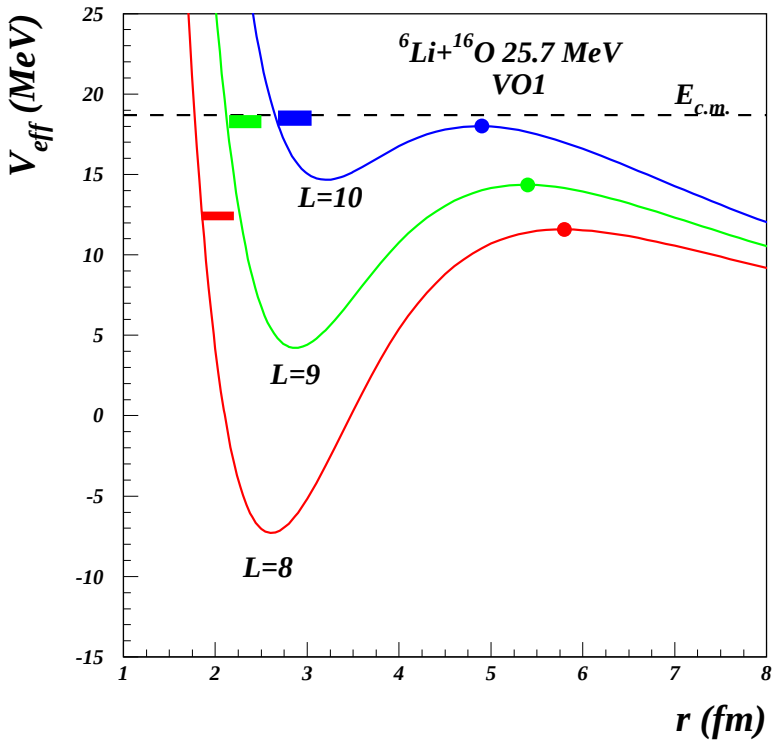

Fig. 19 – (Color online) Shape (molecular) resonances (thick lines) in the effective potential based on VO1 parametrization. Only narrow resonances are shown for a few active partial waves, which are located near the barrier top.

and for $q \neq 0$,

$$S_q(\ell) = (-)^{q+1} \frac{\exp\left[2i(qS_{32} + S_{21} + \delta_1^\ell)\right]}{N^{q+1}(S_{21}/\pi)} \tag{19}$$

In these equations δ_1^ℓ is the WKB (complex) phase shift corresponding to the turning point r_1, $N(z)$ is the barrier penetrability factor,

$$N(z) = \frac{\sqrt{2\pi}}{\Gamma(z+\frac{1}{2})} \exp\left(z \ln z - z\right) \tag{20}$$

and S_{ij} is the action integral calculated between turning points r_i and r_j,

$$S_{ij} = \int_{r_i}^{r_j} dr \{\frac{2\mu}{\hbar^2}[E_{c.m.} - V_{eff} - iW]\}^{1/2} \tag{21}$$

S_{21} and S_{32} are independent of the integration path provided they lie on the first Riemann sheet and collision with potential poles is avoided. Each term in Eq. 17 has a simple physical interpretation. The first term (the barrier term, denoted also

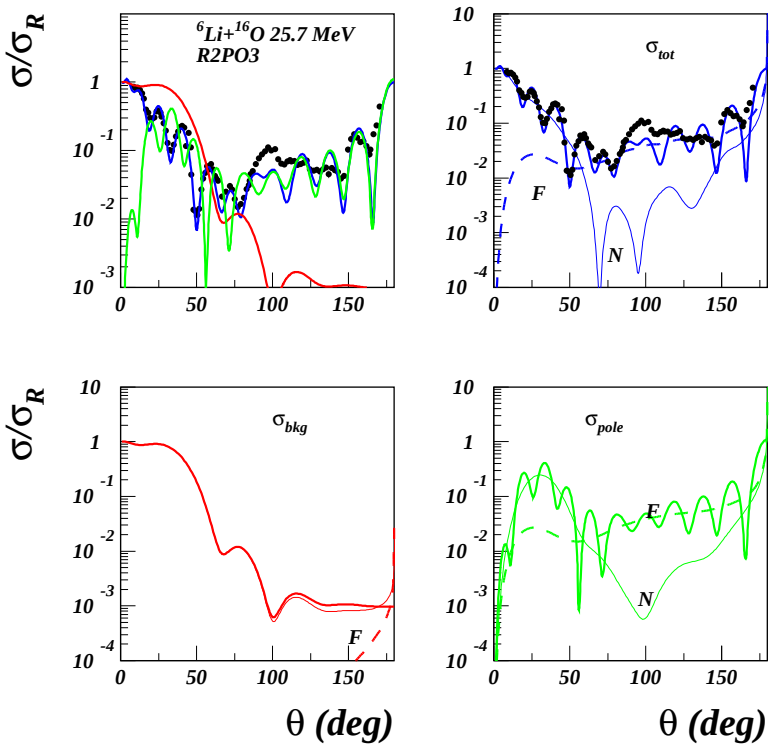

Fig. 20 – (Color online) Comparison of the data with a two Regge pole calculation using parametrization R2PO3. The background σ_{bkg} and pole σ_{pole} components are shown separately. Each component is further decomposed into far and near side.

S_B) retains contributions from trajectories reflected at the barrier, not penetrating the internal region. The qth term corresponds to trajectories refracted q times in the nuclear interior with q-1 reflections at the barrier turning point r_2. Summation of terms $q \geq 1$ can be recast into a single term,

$$S_I = \frac{exp[2i(S_{32}+S_{21}+\delta_1^\ell)]}{N(S_{21}/\pi)^2} \frac{1}{1+\exp\left[2iS_{32}\right]/N(S_{21}/\pi)} \tag{22}$$

and is known as the internal barrier scattering function. When the absorption in the nuclear interior is large, the second factor in the above equation reduces to one and we are left with the expression used in [22]. Since the semiclassical scattering function is decomposed additively, $S_{WKB} = S_B + S_I$, the corresponding total scattering amplitude is decomposed likewise as $f_{WKB} = f_B + f_I$ and conveniently the corresponding barrier and internal barrier angular distributions are calculated as $\sigma_{B,I} = |f_{B,I}|^2$, using the usual angular momentum expansion of the amplitudes.

The accuracy of the semiclassical calculation has been checked by comparing

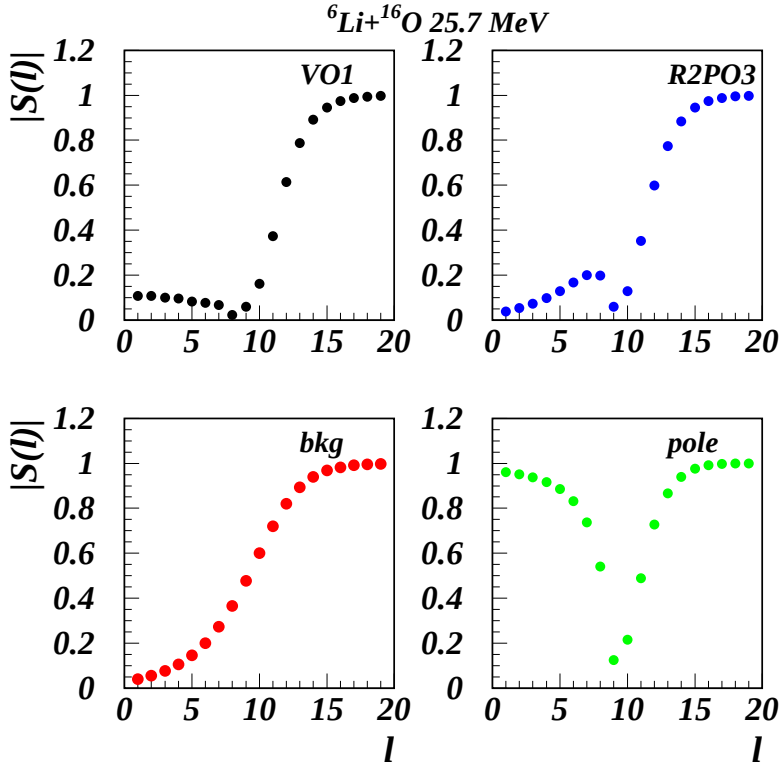

Fig. 21 – (Color online) Absorption profile for the WS potential VO1 compared with the results fro two pole calculation. The Grühn-Wall deep at $l \sim 9$ is due to the pole component in the S-matrix.

the barrier and internal barrier absorption profiles with the exact quantum-mechanical result in Fig. 16. First, one observes that the semiclassical B/I expansion is an $exact$ decomposition of the quantum result. They are virtually identical at the scale of the figure. The internal component gets significant values up to the grazing angular momentum (ℓ_g=12) and is negligibly small beyond this value. The barrier component resembles a strong absorption profile and this justifies the interpretation that it corresponds to that part of the flux not penetrating into the nuclear interior. For values near the orbiting angular momentum ($\ell_o \approx$10), the two components interfere and a downward spike appears in the total profile, in complete agreement with the quantum result. This is the famous Grühn-Wall spike [32] introduced phenomenologically to explain ALAS for α particle scattering, and appears here as a strong interference between barrier and internal barrier amplitudes. Second, the B/I components are almost decoupled in the angular momentum space and therefore they will contribute in different angular ranges.

Semiclassical cross sections are compared with the data in Fig. 17 . Better

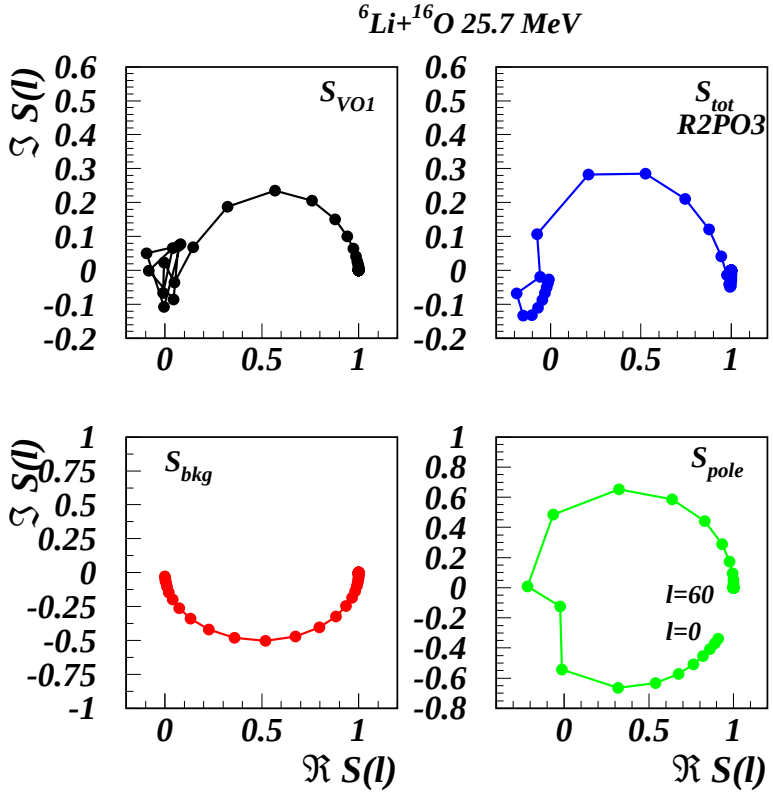

Fig. 22 – (Color online) Argand diagrams for the S-matrix calculated with WS potential VO1 compared with two Regge pole approximation. (parameter set R2PO3).

insight into this technique is obtained by further decomposing the B/I components into far and near (BF/BN and IF/IN) subcomponents. Clearly, the barrier component dominates the forward angle region. Fraunhofer diffractive oscillations appear as the result of BF and BN interference. At large angles, the internal contribution accounts for the full cross section.

Thus, the intermediate angle exotic structure in angular distributions for the elastic scattering of ^{6}Li on ^{16}O can be understood as a result of coherent interference of two far-side subamplitudes generated by different terms in the uniform multireflection expansion of the scattering function (terms q=0 and q=1 in Eq. 17), corresponding to the scattering at the barrier and the internal barrier. This interference effect appears as a signature of a surprisingly transparent interaction potential for loosely bound nucleus ^{6}Li at this low energy which allows part of the incident flux to penetrate the nuclear interior and reemerge with significant probability.

The Argand diagrams corresponding to the B/I decomposition is displayed in

Fig. 18. Evidently, only the internal barrier amplitude is responsible for the resonant behaviour of the low momentum partial waves.

4. REGGE POLES

We have seen in the preceding sections that the data could be described by highly transparent potentials, such that the low absorption is not able to suppress the resonant effects in the low partial waves. Semiclassically, these effects appear as a consequence of multiple reflexions of the internal amplitude between the most internal complex turning points of the potential. A common property of the WS potentials which describe well the data, they all posses several narrow shape (molecular) resonances located in the most active waves $l = 8, 9, 10$ (see Fig.19) In this section we examine this effect in terms of a purely phenomenological Regge pole approximation.

For this purpose we adopt the "product" representation of the S-matrix [19],

$$S(l) = S_{bkg}(l) S_{pole}(l) \tag{23}$$

where the background (bkg) component is borrowed from the strong absorption model of Ericson [33],

$$S_{bkg} = \left[1 + \beta \exp(-i\alpha) \exp\left(\frac{L-l}{\Delta}\right)\right]^{-1} \tag{24}$$

For the pole term we adopt the expression,

$$S_{pole}(l) = \prod_{i=1}^{2} \left[1 + i \frac{D_i(l)}{l - L_i - i\hat{\Gamma}_i(l)/2}\right] \tag{25}$$

This term describes resonances in l centered at L_i with total width $\hat{\Gamma}_i$. In line with McVoy [19] we assume the zeros and the widths slowly l dependent and vanishing small as $l \to \infty$,

$$D_i(l) = \frac{D_i}{1 + \exp(\frac{l-L}{\Delta_i})} \tag{26}$$

$$\hat{\Gamma}_i(l) = \frac{\Gamma_i}{1 + \exp(\frac{l-L}{\Delta_i})} \tag{27}$$

Clearly, D measures the distance between the pole ($p = 1/2\Gamma$) and the zero ($z = 1/2\Gamma - D$). The model has 12 parameters, twice as much as the WS model. The reason is that we were not able to find a single pole unitary solution. Since the problem is highly nonlinear there is no guarantee for the uniqueness of the solution. We used a Monte Carlo procedure to generate input parameters and then minimized

the usual χ^2 objective function. From the numerous solution we found, we choose to show only one set of parameters (Table 4) which has the merit that both S_{bkg} and S_{pole} are unitary. The poles are located in the upper complex l near $L \approx 9,10$, in line with what we found from the other analyses. The cross sections obtained with this model are plotted in Fig.20. The background component is important only at forward angles, while the pole component contributes significantly at all angles. Only the pole component contributes to the far side amplitude which displays only a shallow minimum near $\theta = 50^{\circ}$. The nearby deep minimum, interpreted previously as a Fraunhofer minimum, appears here as a result of the strong destructive interference between far and near side amplitudes of the pole component alone. The background absorption profile shown in Fig.21 is typical for strong absorption regime while the the Grühn-Wall deep appears here as carried out by the pole component alone. The corresponding Argand diagram displayed in Fig. 22 show clearly the resonant contribution of the pole component.

5. CONCLUSIONS

We have analyzed the elastic scattering ^{6}Li+^{16}O at of 4 MeV/A in an effort to obtain systematic information on the interaction of p-shell nuclei with light targets. Optical potentials for these nuclei are needed for studies where highly peripheral transfer reactions involving radioactive nuclei are used as indirect methods for nuclear astrophysics and are an important factor in the accuracy and reliability of these methods. At the present time, the best information on the optical potentials for radioactive nuclei can be obtained only by extrapolation from adjacent less exotic nuclei. Our intention is to narrow the ambiguities in the optical model potentials by systematic studies of the scattering of loosely bound projectiles over a large range of angles and energies, and extract information that can be used for systems involving radioactive projectiles, for which elastic scattering data of very good quality are not easily available.

The data, confirms the existence of an exotic intermediate angle structure, observed previously [4] at higher energy. We interpret these structures as refractive effects arising from a fine balance between the real and imaginary components of the optical potential. We have performed a traditional analysis of the data in terms of Woods-Saxon and microscopic folded potentials. On the other hand a range of effective NN interactions have been used to generate folding potentials. Both approaches lead to the conclusion that the optical potential is deep and surprisingly transparent, in agreement with findings for other more bound systems. Folding model form factors have been renormalized in the usual way in order to account for the energy and radial dependence of the dynamic polarization potential. The intermediate angle structures could be reproduced only with potentials approaching a critical volume

integral of about 280±10 MeV fm^3 and a rms radius $R_V = 4.05 \pm 0.1$ fm and, consequently, are severely selective, limiting the ambiguities in the determination of the OMP. The remaining discrete ambiguities could be removed by including an exact local representation of the knock-on exchange kernel within the Perey-Saxon localization procedure. Our analysis does not confirm the eventuality of a canceling effect between the repulsive dynamic polarization potential due to the coupling with breakup channels and the attractive, dispersive component of the optical potential. As a consequence all folding potentials require a renormalization $N_V < 1$ to match the required critical value of the real volume integral.

The present analysis shows that in order to reproduce the structures observed at intermediate angles in this case, one needs to allow for a more complicated radial dependence of the dynamic polarization potential, which can be energy and target dependent, and requires deep real potentials.

In an effort to clarify the reaction mechanism responsible for the intermediate angle structures, we performed extensive semiclassical calculations within the uniform multireflection expansion of the scattering function of Brink and Takigawa. It has been shown that using complex trajectories, the (external) barrier/internal barrier expansion is an exact realization of the dynamic decomposition of the quantum result into components responsible for that part of the incident flux reflected at the barrier and the part of the flux which penetrates into the nuclear interior and reemerges with significant probability. By combining the B/I decomposition with the usual far-side/near-side expansion, we explain the intermediate angle structure as a coherent interference effect of two subamplitudes (BF and IF). Thus, this refractive effect appears as a signature of a highly transparent interaction potential. This decomposition allows to isolate dynamically the resonant component of the S-matrix which is due to multiple reflections of the low angular momentum waves between the most internal complex turning points of the potential.

A completely different picture emerges by using a slight generalization of the "product" Regge pole representation of the full S-matrix. Seeking for a unitary solution, we found that the pole component is entirely responsible for the intermediate angle structure and the oscillatory behaviour of the cross section at large angles. Thus it is a matter of taste if we interpret intermediate angle structure as a resonant refraction of equally well as a resonant diffraction.

Acknowledgments. This work was supported in part by CNCSIS-Romania Grants PN-II-ID-PCE-2011-3-0427 and 0554 and by the U. S. Department of Energy under Grant No. DE-FG02-93ER40773 and by the Robert A. Welch Foundation. We are grateful to dr. M. F. Vineyard for sending us his data in tabular form.

REFERENCES

1. G. R. Satchler and W. G. Love, Phys. Rep. **55**, 183 (1979).
2. M. E. Brandan and G. R. Satchler, Phys. Rep. **285**, 143 (1997).
3. L. Trache, A. Azhari, H. L. Clark, C. A. Gagliardi,Y.- W. Lui, A. M. Mukhamedzhanov, R. E. Tribble and F. Carstoiu, Phys. Rev. C **61**, 024612 (2000).
4. F. Carstoiu, L. Trache, R. E.Tribble, C. A. Gagliardi, Phys. Rev. C **70**, 054610 (2004).
5. A. A. Ogloblin *et al.*, Phys. Rev. C **62**, 044601 (2000).
6. S. Szilner *et al.*, Phys. Rev. C **64**, 064614 (2001).
7. E. Stiliaris *et al.*, Phys. Lett. **B223**, 291 (1989).
8. J. Knoll and R. Schaeffer, Ann. Phys. (N.Y.) **97**, 307 (1976).
9. R. Anni, Phys. Rev. C **63**, 031601R (2001).
10. H. Feshbach, Ann. Phys.(N. Y.) **5**, 357 (1958); **19**, 287 (1962).
11. Y. Sakuragi, Phys. Rev. C **35**, 2161 (1987).
12. C. Mahaux, H. Ngo and G. R. Satchler, Nucl. Phys. **A449**, 354 (1986).
13. A. Nadasen *et al.*, Phys. Rev. C **37**, 132 (1988).
14. A. Nadasen *et al.*, Phys. Rev. C **47**, 674 (1993).
15. D. E. Trcka, A. D. Frawley, K. W. Kemper, D. Robson, J. D. Fox and E. G. Myers, Phys. Rev. C **41**, 2134 (1990).
16. M. F. Vineyard, J. Cook, K. W. Kemper, M. N. Stephens, Phys. Rev. **C30**, 916 (1984) and private communication.
17. J.P. Jeukenne, A. Lejeune and C. Mahaux, Phys. Rev. C **16**, 80 (1977).
18. D. M. Brink and N. Takigawa, Nucl. Phys. **A279**, 159 (1977).
19. K. W. McVoy, Phys. Rev. C **3**, 1104 (1971).
20. M.S. Hussein and K.W. McVoy, Nucl. Phys. **A445**, 123 (1985).
21. A. Bonaccorso and F. Carstoiu, Nucl. Phys. **A706**, 322 (2002).
22. F. Michel, G. Reidemeister and S. Ohkubo, Phys. Rev. Lett. **89**, 152701 (2002); *ibidem*, Phys. Rev. C **63**, 034620 (2001).
23. R. M. Drisko, G. R. Satchler and R. H. Bassel, Phys. Lett. **5**, 347 (1963).
24. M. Beiner and R. J. Lombard, Ann. Phys. **86**, 262 (1974).
25. I. Angeli, Heavy Ion Physics **8**, 23 (1998).
26. N. Anantaraman, H. Toki, G. F. Bertsch, Nucl. Phys. **A398**, 269 (1983).
27. J. W. Negele and K. Yazaki, Phys. Rev. Lett .**47**, 71 (1981).
28. Ş. Mişicu and F. Carstoiu, Phys. Rev. C **83**, 054622 (2011).
29. D. Gogny, Proc. Int. Conf. on Nucl. Phys., Munich 1973, eds. J. de Boer and H. J. Mang.
30. P. Fröbrich and R. Lipperheide, *Theory of Nuclear Reactions* (Clarendon Press, Oxford, 1996).
31. K. W. Ford and J. A. Wheeler, Ann. Phys. (N. Y.) **7**, 259 (1959).
32. C. R. Grühn and N. S. Wall, Nucl. Phys. **81**, 161 (1966).
33. T. E. O. Ericson, Preludes in Theoretical Physics, eds, A. de-Shalit, L. Van Hove and H. Feshbach, North Holland, 1965.

Table 1.

Best fit Woods-Saxon parameters. Reduced radii are defined in the heavy ion convention. Coulomb reduced radius is fixed to r_c=1 fm. R_V and R_W are the rms radii of the real and imaginary potentials, respectively. The normalized χ^2 is calculated assuming uniform 10% error.

Pot.	V_0 [MeV]	W_0 [MeV]	r_V [fm]	r_W [fm]	a_V [fm]	a_W [fm]	χ^2	σ_R [mb]	J_V [MeV fm^3]	R_V [fm]	J_W [MeV fm^3]	R_W [fm]
VO1	162.21	5.02	0.53	1.47	0.993	0.654	9.81	1434	248	4.087	63	5.502
VO2	224.00	5.98	0.54	1.41	0.911	0.687	9.27	1430	318	3.839	68	5.397
VO3	282.22	7.00	0.57	1.37	0.844	0.719	9.59	1436	402	3.670	73	5.319
VO4	350.50	8.24	0.58	1.31	0.796	0.755	10.13	1438	496	3.551	78	5.229

Table 2.

Best fit JLM parameters. The notations are those from the text.

Pot.	t_V [fm]	t_W [fm]	N_V	N_W	χ^2	σ_R [mb]	J_V [MeV fm^3]	R_V [fm]	J_W [MeV fm^3]	R_W [fm]
JLM1O-1	1.663	2.580	0.309	0.374	14.8	1429	200	4.314	56	5.162
JLM1O-2	1.096	2.959	0.417	0.389	13.1	1533	271	4.029	59	5.327
JLM1O-3	0.646	2.795	0.543	0.429	11.5	1513	354	3.879	64	5.327
JLM1O-4	0.136	2.652	0.685	0.474	14.0	1521	452	3.801	71	5.216
JLM3O-1	1.148	2.998	0.452	0.488	13.5	1541	269	4.021	58	5.485
JLM3O-2	0.733	2.763	0.588	0.532	11.6	1509	351	3.871	64	5.296
JLM3O-3	0.097	2.696	0.710	0.591	12.8	1525	442	3.767	71	5.243
JLM3O-4	0.090	3.523	0.890	0.757	21.3	1816	555	3.766	90	5.938
GOGNY-1	0.383	2.944	0.426	0.092	12.6	1540	284	4.072	60	5.427
GOGNY-3	0.083	2.844	0.520	0.114	12.3	1534	289	4.100	61	5.386

Table 3.

Best fit FLDD and M3Y parameters. The notations are those from the text.

Pot.	t_V [fm]	t_W [fm]	N_V	N_W	χ^2	σ_R [mb]	J_V [MeV fm^3]	R_V [fm]	J_W [MeV fm^3]	R_W [fm]
FO1	1.969	3.026	-186.4	-53.3	14.6	1438	199	4.315	56	5.189
FO2	1.500	3.378	-248.3	-54.5	14.6	1542	266	4.019	57	5.479
FO3	1.182	3.163	-320.5	-58.9	12.8	1508	344	3.856	62	5.282
FO4	0.887	3.078	-400.0	-64.9	12.8	1513	431	3.733	68	5.205
M3YZR1	1.491	2.739	0.438	0.125	14.6	1438	199	4.315	56	5.159
M3YZR2	0.778	3.127	0.584	0.128	14.6	1463	266	4.022	57	5.482
M3YZR3	0.090	2.799	0.737	0.139	14.4	1499	352	3.908	62	5.208
M3YZR4	0.104	3.890	0.950	0.196	24.9	2025	451	3.908	87	6.177
M3YFR1	1.245	2.657	0.357	0.103	15.1	1463	202	4.313	58	5.190
M3YFR2	0.364	2.904	0.492	0.105	13.3	1532	279	4.056	59	5.387
M3YFR3	0.093	3.585	0.641	0.138	22.2	1877	380	4.034	77	5.974
M3YFR4	0.108	4.126	0.840	0.173	27.3	2238	494	4.035	96	6.480
M3YFR6	0.321	2.956	0.490	0.106	13.2	1536	278	4.052	59	5.429
M3YFR7	1.249	2.635	0.358	0.103	14.9	1447	202	4.315	57	5.173

Table 4.

Parameters for a two Regge pole unitary solution. The first 4 columns define the background S-matrix and the next ones define the pole component. The approximate pole and zero positions predicted by the model in the complex l-plane are given by $L_i + ip_i$ and $L_i + iz_i$ respectively. See text for notations

Set	L	Δ	α	β	L_1	Δ_1	D_1	Γ_1	L_2	Δ_2	D_2	Γ_2	χ^2	σ_R
R2PO3	14.73	3.08	-1.57	0.29	9.82	1.72	3.10	5.03	8.97	1.02	0.41	1.19	4.32	1437